Silver Decorated TiO_2 Inverse Opal Structure for Visible Light Induced Photocatalytic Degradation of Organic Pollutant and Hydrogen Evolution

Filipp Temerov[1*], Khai Pham[1], Paxton Juuti[2], Jyrki M. Mäkelä[2], Elena V. Grachova[3], Santosh Kumar[4], Salvador Eslava[4] and Jarkko J. Saarinen[1]

[1]*Department of Chemistry, University of Eastern Finland, P.O. Box 111, FI-80101 Joensuu, Finland*

[2]*Aerosol Physics Laboratory, Physics Unit, Tampere University, P.O. Box 692, FI-33101 Tampere, Finland*

[3]*Institute of Chemistry, St. Petersburg State University, 198504 St. Petersburg, Russian Federation*

[4]*Department of Chemical Engineering, Imperial College London, London, SW7 2AZ, United Kingdom*

**Corresponding author*

Abstract

TiO_2 inverse opal (TIO) structures were prepared by conventional wet chemical method resulting in well-formed structures for photocatalytic activity. The obtained structures were functionalized with liquid flame spray (LFS) deposited silver nanoparticles (AgNPs). The nanocomposites of TIO and AgNPs were extensively characterized by various spectroscopies such as UV, Raman, XRD, EDS, and XPS combined with microscopic methods such as SEM, TEM, and HRTEM. The characterization confirmed that high quality heterostructures had been fabricated with evenly and uniformly distributed AgNPs. Fabrication of anatase TiO_2 was confirmed as well as formation of AgNPs was verified with surface plasmon resonant (SPR) properties. The photocatalytic activity results measured in gas-phase showed that deposition of AgNPs increase photocatalytic activity both under UVA and visible light excitation, moreover enhanced hydrogen evolution was demonstrated under visible light.

Key words

TiO_2 inverse opal; Silver nanoparticles; Photocatalysis; Liquid flame spray, Hydrogen evolution

1 Introduction

The Intergovernmental Panel on Climate Change (IPCC) released a report (2018/10) revealing the current state of the climate change with constantly growing CO_2 level.[1] To limit the temperature increase of the planet to 1.5°C requires a major transformation of the energy sector, with the main CO_2 source being the combustion of fossil fuels. A partial replacement of fossil fuels has already taken place by wind, hydro, nuclear, and solar energy. However, these methods cannot fully replace the use of fossil fuels. Harvesting solar energy by solar cells has been widely studied since 1950s,[2] and today the best available solar power conversion efficiencies with multijunction solar cells reach almost 50%.[3] An alternative approach of solar energy exploitation is the use of TiO_2 to photocatalytically store the solar energy in chemical bonds of fuels such as hydrogen upon redox reactions of water. TiO_2 is a non-toxic and widely used white pigment with good photostability which could ensure mass production of solar devices.[4]

However, TiO_2 in anatase crystalline phase has major drawbacks, which limit its utilization in solar light photocatalysis, such as rather wide band gap energy 3.2 eV[5,6] and high recombination rate of photogenerated electron–hole pairs.[7] Several strategies have been developed to mitigate these drawbacks, such as functionalizing TiO_2 with various nanostructures.[8,9] TiO_2 nanoparticles functionalized with silver nanoparticles (AgNPs) have been used for enhanced photocatalytic activity as they allow visible light activation through localized surface plasmon resonance phenomenon (LSPR). Additionally, AgNPs also decrease the recombination of photogenerated electron-hole pairs.[10] The TiO_2 photocatalytic activity can also be improved designing specific shapes and morphologies, such as nanobelts,[11] nanotubes,[12] nanorods,[13] nanosheets,[14] multilayer structures,[15] and inverse opals (IOs).[16–18] Combining the functionalization of nanoparticles and the IO morphology, the photocatalytic activity of TiO_2 inverse opals (TIO) can be enhanced by decoration with noble metals such as silver,[19] gold,[20] platinum[21] or graphene-based materials.[22] Today, hierarchical structures such as inverse opals gain more interest due to their novel properties such as photonic band gap (PBG), slow light photon effect, and localized photons.[23,24] The TIO structure consists of a three-dimensional ordered porous structure with a large specific surface area, and it can display an enhanced photocatalytic activity compared to TiO_2 nanoparticles due to slow photons with energies close to the PBG of the semiconductor.[25]

AgNPs have been shown appropriate for industrial-scale applications due to low cost and simple preparation. AgNPs are efficient at absorbing and scattering light, and they show a color appearance depending on the size and shape of the particle. Conduction band electrons on the AgNPs surface

undergo a collective oscillation by light that is known as a surface plasmon resonance (SPR). Therefore, AgNPs can have effective extinction (scattering + absorption) cross-sections up to ten times larger than their physical cross-sections.[26] Traditionally, AgNPs are deposited onto TiO_2 photocatalysts by conventional photochemical reduction method by UV light.[27] However, this method has several disadvantages such as weak bonds between the metal nanoparticles and TiO_2, poor repeatability, and tendency to form nanoparticle agglomerates on the TiO_2 surface. A large diversity of deposition methods such as hydrothermal reduction,[28] atomic layer deposition,[29] spin coating,[30] evaporation method,[19] and pulsed current deposition[31] have also been reported.

Recently, liquid flame spray (LFS) nanoparticle deposition method has received large attention due to its high deposition speed, uniform and porous deposition, as well as low cost. LFS is based on a hydrogen-oxygen flame in which an organometallic precursor is fed into. In the flame, the precursor undergoes evaporation followed by nucleation and formation of solid nanoparticles which are, furthermore, deposited onto the surface due to the high thermal gradient between the flame and the surface. LFS has been utilized for various nanoparticles such as TiO_2,[32] SiO_2[33] and Ag.[34] The LFS deposition parameters can be used to control the deposition of nanoparticles with variable size and amount on selected substrate materials. Compared to the existing methods such as the atomic layer, chemical vapor, or pulsed current deposition[31] of nanoparticles, the LFS process has a number of benefits such as easy operation at atmospheric conditions, high deposition rate, and cost-effective deposition suitable also for roll-to-roll process flow.[35]

In the present work, we demonstrate a facile deposition of AgNPs by LFS on a TIO structure for enhanced photocatalytic activity. Our experimental results demonstrate that resulting TIOAg structures show both UV and visible light activation compared with TIO. The photocatalytic activity was measured in the decomposition of organic contaminants in an in-house built gas-phase reactor.[19,36] Acetylene is present in automobile exhausts; hence, it was chosen as a test analyser for this work. This gas photocatalytic method has several advantages over liquid phase methods such as absence of mechanical stresses on the nanostructures and bleaching prevention of dyes by incident light. The mineralization of carbon compounds into CO_2 was directly measured with an optical detector in the reactor. Furthermore, the photocatalytic activity of these TIOAg structures for water vapor splitting to generate hydrogen gas was evaluated, showing again the benefits of LFS of AgNPs on TIO structures.

2 Results and discussion

2.1 Preparation and characterization of TIOAg nanocomposites

TIO structures were prepared by self-assembling polystyrene (PS) spheres on microscopic glass slides by slow vertical deposition. It is well-known that PBG has a strong influence on the photocatalytic properties of TIO structures. If the plasmonic band of AgNPs is inside the PBG, the incoming light will be absorbed solely by AgNPs and reflect from the IO structure followed by a reduced photocatalytic activity. In the current work, one particle size (350 nm) was used to achieve the plasmonic band of AgNPs outside the red edge of the PBG. Hence, an increased photocatalytic activity can be expected upon AgNPs deposition by LFS method. Figures 1A and S1 show the scanning electron microscopy (SEM) micrographs of the PS sphere colloidal crystal templates. The average size of the PS spheres is 350 nm, which was selected for their excellent reproducibility for the production of TIO structures. The SEM micrograph clearly demonstrates a well-ordered close packed PS spheres with a high degree of order displaying a face-centered cubic (FCC) plane (1 1 1) orientation. TIO structures were obtained after infiltration of a Ti based precursor, hydrolysis, and calcination at 500°C. Figure 1B includes the top-view SEM micrograph of the TIO, which shows an even and uniform sample morphology with no observable cracks. Based on the SEM analysis, the used PS template was removed completely and overlayers of TiO_2 based precursors were not present. Although SEM analysis showed no PS template or TiO_2 precursors remaining, a recent XPS study reported that calcination (at 500 °C) may not fully remove the used PS template and residual carbon can be trapped into the structure.[37] The average pore size in the TIO is 200-250 nm, which indicates a PS sphere shrinkage of approximately 28-42% during the high-temperature calcination.[31]

The TIO surface was used as a substrate for the deposition of AgNPs by liquid flame spray (LFS) method. An Ag liquid precursor was fed into a nozzle, and the formation of nanoparticles took place in the flame. The LFS nanoparticles were deposited using a rotating carousel, in which the number of deposited nanoparticles was simply controlled by the number of times the glass slides with TIO pass through the flame (from 5 to 30 times). Figure 1C-F show SEM micrographs of TIOAg 5x, 10x, 20x, and 30x, respectively. It can be clearly seen that the deposition process does not damage the TIO surface since the structures with deposited NPs have the same morphology as the pristine TIO. This highlights the short exposure time to the flame. The average size distribution of AgNPs was analyzed in the SEM micrographs (Figure S2). The average diameter of the TIOAg5x is 25–35 nm (Figure 1C), and it increases to 55–65 nm for TIOAg10x (Figure 1D). The size further increases to 65–75 nm and 80–90 nm for 20x and 30x, respectively (Figure 1E and 1F, respectively). It was observed that the AgNPs do not block the pores and mainly deposit on the ridges of the top rows of pores. Finally, low magnification SEM micrographs of TIOAg were obtained, confirming the quality of the IO structures with AgNPs even distribution (Figure S3).

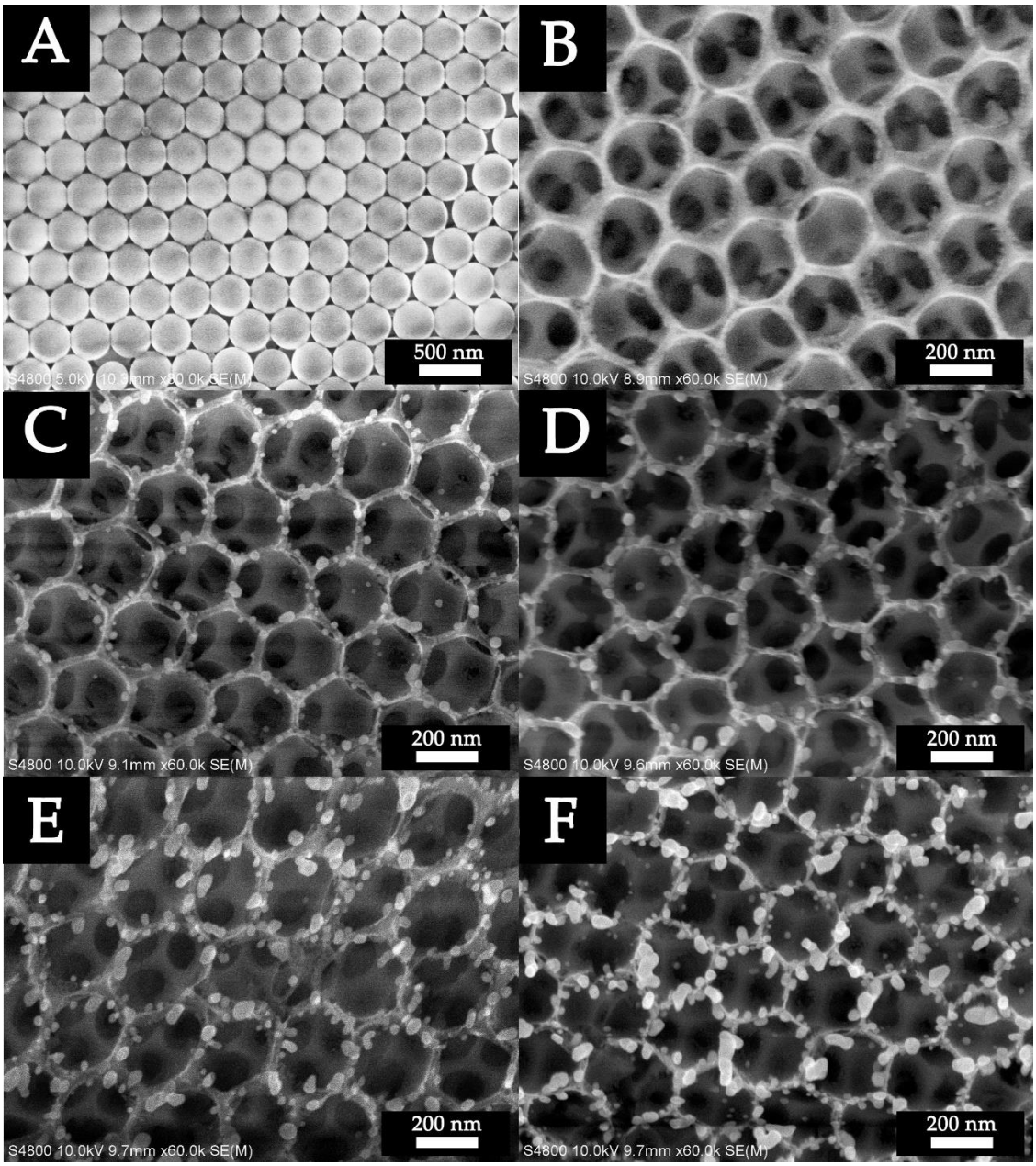

Figure 1. SEM micrographs of (A) polystyrene (PS) self-assembled spheres, (B) TIO without AgNPs, (C) TIOAg5x, (D) TIOAg10x, (E) TIOAg20x, and (F) TIOAg30x.

Energy dispersive spectroscopy (EDS) mapping analysis was performed to confirm the composition of the TIOAg samples. Figure 2 illustrates a typical EDS mapping profile obtained for TIOAg30x that clearly indicates that structure consisting of titanium and oxygen (green and blue dots) whereas red islands indicate the location of AgNPs. Furthermore, the EDS spectrum was also obtained for a complete compositional analysis (Figure S4), reinforcing mapping profiles results.

The distribution of AgNPs on TIO structure was further studied by HRTEM microscopy. Figure 3 shows HRTEM micrographs of Ag nanoparticles anchored onto the TIO. The lattice fringes with a d-spacing of 0.352 and 0.224 nm represented the (1 0 1) plane of anatase TiO_2 and the (1 1 1) plane of metallic AgNPs, respectively. The micrographs confirm the highly crystalline structure of TIOAg nanocomposites and highly uniform distribution of AgNPs. Moreover, the LFS method provides a more even distribution than an infiltration method.[20]

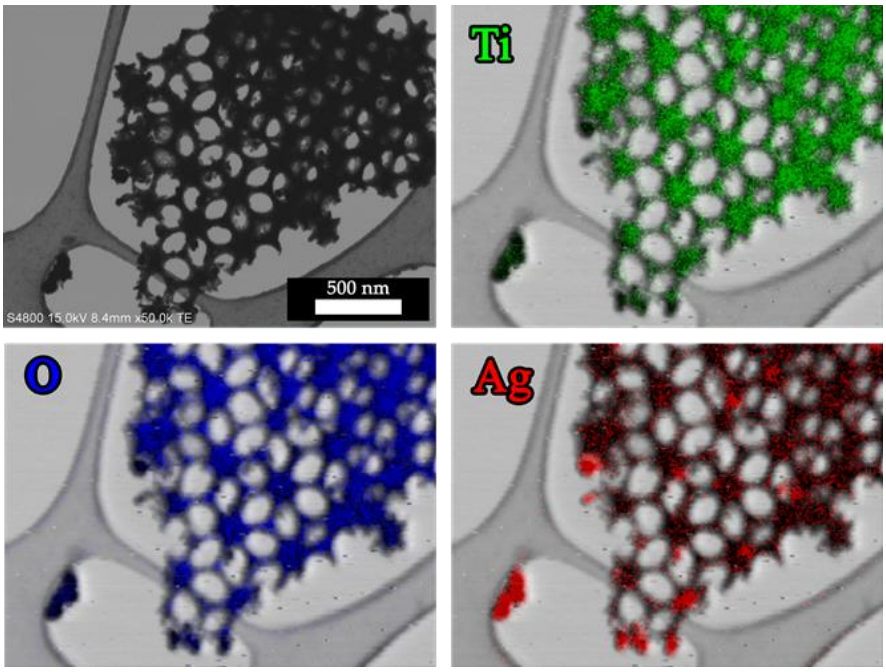

Figure 2. EDS mapping TEM micrographs of TIOAg30x.

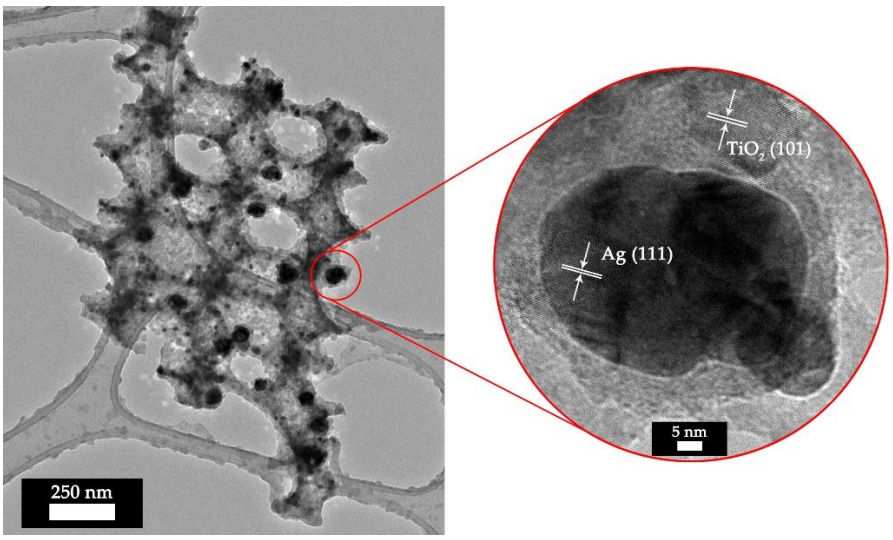

Figure 3. HRTEM micrograph of TIOAg30x interface between TiO_2 and AgNPs.

For photocatalytic applications, the stopbands of TIO structures can be calculated using Bragg's law

$$\lambda_{max} = \frac{2D\sqrt{2}}{\sqrt{3}}\sqrt{n_{TiO2}^2 f + n_{air}^2(1-f) - sin^2\theta} \quad (1)$$

where λ_{max} is the stopband position for the first order Bragg diffraction; D is the pore size of TIO; n_{TiO2} and n_{air} are the refractive indexes and can be taken as 2.5 and 1.0003, respectively; f is the TIO phase volume percentage of 0.26 based on the FCC geometry,[18,31] and θ is the incident angle of light, which is 0° in these experiments. According to the Eq. (1), the stop band of the TIO was found in the range of 500-630 nm assuming an average pore diameter around 200-250 nm that agrees well with the observed TIO absorbance spectrum (Figure 4).

The normalized UV–vis diffuse absorbance spectra of TIOAg were measured normal to the FCC (1 1 1) plane as shown in Figure 4. TIO without nanoparticles exhibits broad PBG in the range of 380–600 nm (red area) due to slow photon effects that allow multiple light scattering and improvement of the light harvesting and intrinsic band gap absorbance of TiO_2 starting from 370 nm until it achieves a maximum deep in the UV range. Deposition of AgNPs induces more extensive absorbance of visible light due to plasmonic excitation of metal nanoparticles combined with slow light effect of the IO structure.[31] The absorbance reaches its maxima in TIOAg30x in the visible range. Additionally, a new peak appears at 375 nm (blue area) in TIOAg20x and TIOAg30x due to a quadrupole resonance effect in AgNPs.[38] An increased PBG with a redshift was observed with increased AgNPs deposition amounts. This phenomenon may result from the PBG position of TIO that is affected by the redox states of the AgNPs, namely the plasmon absorption of AgNPs that can lower the reflectance intensity of the TIO whereas Ag_2O does not affect it. The UV/Vis light irradiation can induce reversible changes in the intensity of the PBG due to the photoinduced reversible transformation between AgNPs and Ag_2O.[39] These two processes may result in the observed redshift of the PBG in TIOAg nanocomposites. Notably, the red edge of the PBG in TIO (Figure 4) does not overlap with the plasmonic bands of AgNPs (Figure S5) providing an optimal condition for photocatalytic reactions.

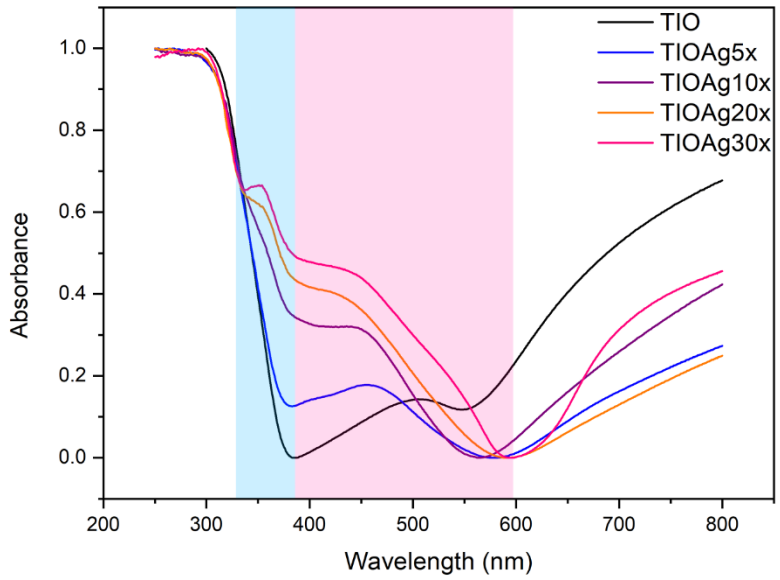

Figure 4. Normalized UV–vis diffuse absorbance spectra of TIOAg structures.

Raman spectroscopy was used to characterize TIOAg structures. Figure 5A displays characteristic anatase bands in all samples. The peak at 145 cm^{-1} is assigned to E_{g1} O−Ti−O bond bending vibration and peaks at 196, 395, 516, and 639 cm^{-1} corresponded to E_{2g}, B_{1g}, A_{1g}, and E_{g3} Ti−O−Ti bending, respectively.[40] A new band appeared at 230 cm^{-1} as the AgNPs amount increased that corresponds to a bending vibration mode of Ag–OCO–.[41] This peak clearly indicates that the main interaction of the TiO_2 with the Ag surface is through carboxylic groups, i.e. by Ag–OCO interaction. The band is observed in TIOAg20x and TIOAg30x samples, whereas TIOAg samples with lower AgNP amount do not have this peak indicating that Ag–OCO– may form during the LFS deposition process. The source for the observed carbon peak is probably the used TIO substrate. It has been shown recently[37] that calcination does not fully remove the used carbon template (PS spheres in our case). Hence, the residual carbon left from calcination may evaporate and form volatile carbonic compounds under the heat of the flame that are deposited on top of AgNPs. The accumulated carbon is thus observable for AgNPs deposition with higher amounts of 20x and 30x.

X-ray diffraction (XRD) patterns for the TIO and TIOAg are presented in Figure 5B. The characteristic peaks correspond to the anatase crystalline phase of TiO_2 at 2θ = 25.3° (1 0 1), 37.8° (0 0 4), 48.0° (2 0 0), 53.9° (1 0 5), 55.1° (2 1 1), 62.7° (2 0 4), 68.7° (1 1 6), 70.3° (2 2 0), and 75.0° (2 1 5). These patterns confirm a successful hydrolysis and calcination process. Moreover, the results are well correlated with the Joint Committee on Powder Diffraction Standards File number JCPDS 21-1272, displaying a body centered tetragonal phase. The XRD patterns clearly indicate that no other crystalline phases but just anatase is present. The diffraction peaks at 2θ = 38.1° (1 1 1), 44.3° (2 0 0), 64.4° (2 2 0), and 77.4° (3 1 1) correspond to the LFS deposited AgNPs with a face centered cubic

(FCC) plane, which correlate well with previous studies (JCPDS 04-0783).[42] The intensity of the Ag diffraction peaks increases with the number of Ag deposition times. However, TIOAg5x and TIOAg10x do not show any peaks that correspond to AgNPs, probably due to a low NP amount. This agrees well with Raman spectroscopy analysis, where only two samples showed peaks assigned to AgNPs. Moreover, diffraction peaks also confirm the crystallinity of AgNPs that is an important parameter promoting visible light photoexcitation of electrons and holes. The coherent diffraction domain sizes of both TiO_2 and AgNPs were calculated from Scherrer's equation:

$$D = \frac{k\lambda}{\beta cos\theta} \tag{2}$$

where *D* is the coherent diffraction domain size (nm), herein referred as crystallite size for readability, *k* is the shape constant (that can be taken as 0.9), λ is the wavelength of Cukα radiation (1.5406 Å), β is the full width at half maximum, and θ is the diffraction angle. The crystallite size of the anatase was calculated to be approximately 20 nm. Furthermore, the same crystallite size was found for all samples indicating that the deposition of AgNPs does not affect the crystallinity of TiO_2. The crystallite size of the AgNPs was also calculated. The computed results were 68.4 nm and 80.6 nm for TIOAg20x and TIOAg30x, respectively. These results are in good agreement with SEM results (Figure 1).

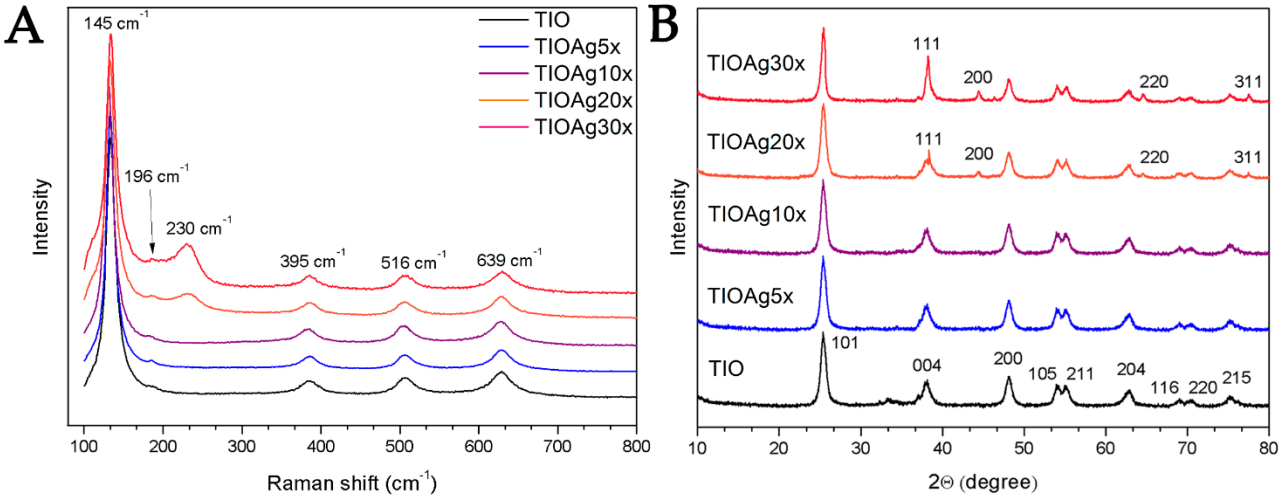

Figure 5. (A) Raman spectra and (B) X-ray powder diffraction (XRD) patterns of TIOAg structures.

High-resolution X-ray photoelectron spectroscopy (XPS) analysis was performed for chemical composition characterization and confirmation of an effective integration of AgNPs on the TIO (Figure 6). The survey scan XPS spectrum has four major peaks from the C 1s, O 1s, Ti 2p, and Ag 3d in the TIOAg30x sample (Figure 6A). The presence of C 1s agrees with the Ag–OCO– observed

upon LFS deposition. Two XPS peaks of Ti $2p_{3/2}$ and Ti $2p_{1/2}$ were recorded at the binding energies of 459.0 and 465.0 eV (Figure 6B), which indicate Ti^{4+} state.[31,43] Two XPS oxygen species were recorded at the O 1s spectrum (Figure 6C), one with binding energy of 530.0 eV corresponding to the lattice oxygen of TiO_2 and other with binding energy of 532.2 eV corresponding to adsorbed oxygen and/or surface hydroxyl species (i.e. Ti−OH).[44] Figure 6D shows a high resolution XPS spectrum for the Ag 3d. The Ag $3d_{5/2}$ peak is found at 368.0 eV and the Ag $3d_{3/2}$ peak at 374.0 eV. The difference between the binding energy of Ag $3d_{5/2}$ and $3d_{3/2}$ was 6.0 eV that confirmed the metallic nature of Ag 3d state.[45]

The three other TIOAg samples were also characterized by XPS (Figure S6), showing the same nature of results. Overall, results obtained from SEM, HRTEM, EDS and XPS support an excellent interaction between AgNPs and TiO_2 IOs.

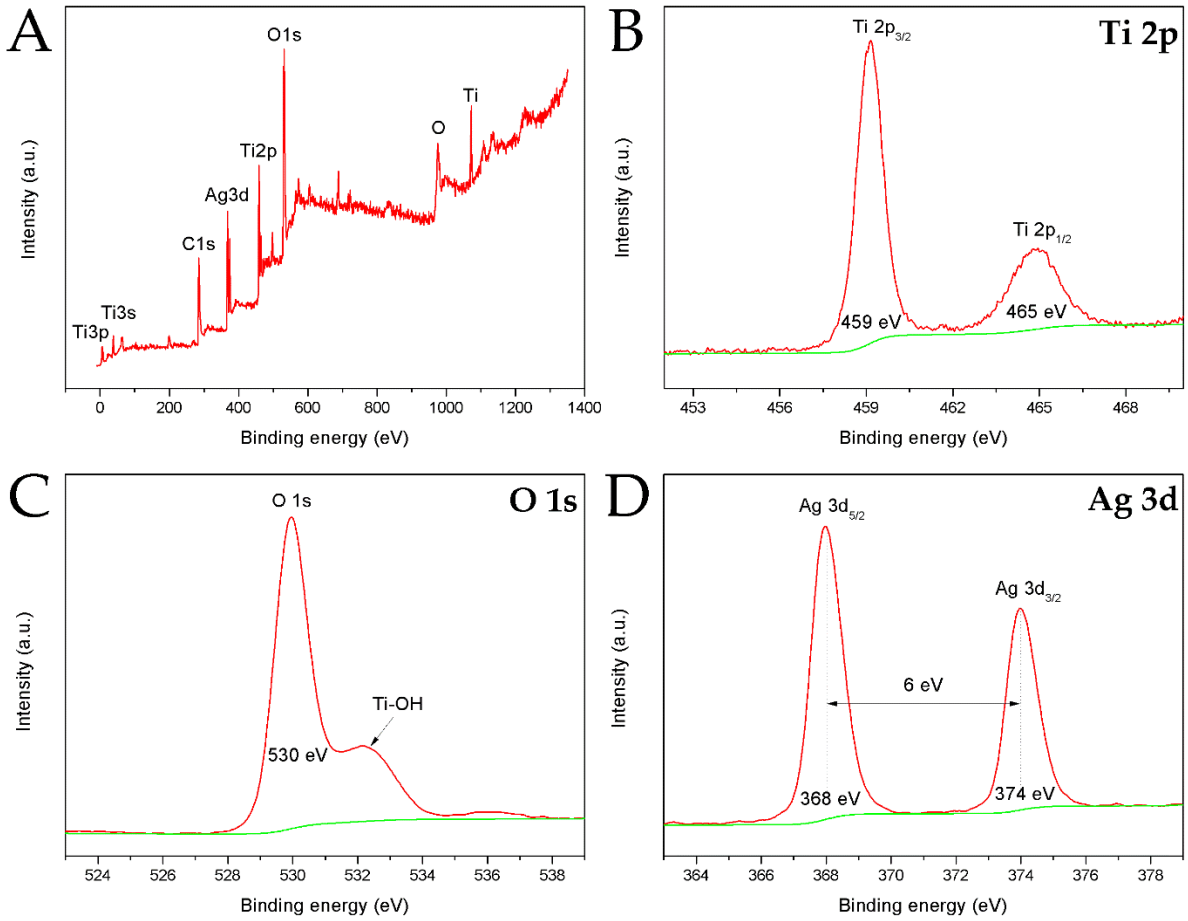

Figure 6. Survey scan XPS spectrum (A) and high resolution XPS spectra of (B) Ti 2p, (C) O 1s, (D) Ag 3d of TIOAg30x.

2.2 Photocatalytic activity and hydrogen evolution of TIOAg nanocomposites

The photocatalytic activities of TIO and TIOAg solid samples were examined in gas systems (Figure S7) under both full source spectrum (unfiltered Xe lamp light) and > 390 nm filtered Xe lamp light (filtered light). Gaseous photocatalytic reactors with a solid photocatalyst have a number of advantages such as absence of mechanical stress on the photocatalyst, unlike traditional solution-based photocatalytic reactors where solid photocatalysts and optical dyes are dispersed/dissolved into a liquid. More importantly, the typically used dyes can be bleached by the incident light itself and thus induce an invalid result of photocatalytic activity.[46] Gas-phase photocatalytic reactors have been intensively investigated in earlier works displaying a clear benefit compared to solution based reactors.[36,47,48] The photocatalytic activities of all our samples were recorded at different times by monitoring the photocatalytic degradation of C_2H_2 under irradiation. Figure 7A represents the results of photodegradation of C_2H_2 to CO_2 in the presence of unfiltered Xe lamp (i.e. UV-Vis). TIO without AgNPs has the lowest activity (1.86 ppm min^{-1}). The observed photocatalytic activity of TIO was higher compared with individual TiO_2 NPs prepared by LFS (Figure S8) due to the ordered anatase crystalline form of TIO structures having a unique optical property that can promote enhanced light absorption and utilization by slow photon effect.[49] The improvement of photocatalytic activity or photodecomposition of C_2H_2 into CO_2 was demonstrated upon incorporation of AgNPs5x. It is worth mentioning that AgNPs were deposited on the first layers of the TIO, which are the ones involved in the photocatalytic reactions since TiO_2 has a high extinction coefficient.[50] It is clearly seen that even a relatively small amount of noble metal nanoparticles is enough to boost the photocatalytic activity performance. TIOAg5x increased photocatalytic activity by 50 % (to 2.78 ppm min^{-1}) compared with TIO without AgNPs. Further LFS deposition cycles to 10x, 20x, and 30x resulted in an increase of the photocatalytic activity by 67 % (to 3.09 ppm min^{-1}), 91 % (to 3.55 ppm min^{-1}), and 106 % (to 3.82 ppm min^{-1}), respectively. Further deposition of AgNPs on TIO was not carried out to avoid sizes larger than 100 nm, which would decrease the photocatalytic activity due to an excess of scattering of light and blockage of pores (the average TIO pore size is 200-250 nm).

Photocatalytic activity was also evaluated using a 390 nm filter that blocks the <390 nm UV light, so only >390 nm light (most is visible light) reaches the photocatalyst (Figure 7B). TIO without AgNPs did not show any activity due to the large band of TiO_2 anatase (3.2 eV, 387 nm).[5,6] However, addition of AgNPs induced photocatalytic activity with the visible light (>390 nm): TIOAg5x had an activity of 0.38 ppm min^{-1}, which increased for TIOAg10x, 20x, and 30x to 0.48, 0.7 and 0.86 ppm min^{-1}, respectively. Photocatalytic activity is significantly smaller when the <390 nm UV light is filtered from the Xe lamp spectrum. For example, TIOAg30x has 4.5 times higher photocatalytic activity

under the full spectrum compared with just the >390 nm light. The observed photocatalytic activity under mainly visible light can be explained by a synergistic action of AgNPs and TIO structures. As mentioned before, AgNPs enhance visible light absorption due to plasmonic coupling followed by electronic interaction and slow light effect of TIO structures. Furthermore, stability of TIOAg30 was investigated by reusability tests with unfiltered light (Figure7C and 7D). It was observed that TIOAg30x does not exhibit significant loss of activity after three cycles (90 min). Table S1 summarizes the comparison of photocatalytic performance of previously reported TiO_2 IO based photocatalysts under visible light irradiation.

All samples were calcined at 500℃ for the removal of PS particles and formation of the TIO structures. The calcination temperature can affect the photocatalytic activity, since the temperature determines the final crystallite grain size, the surface area, and the crystallinity. The crystalline grain sizes were estimated by HRTEM for TIOAg30x (Figure S9) were found to be within 20-30 nm, in agreement with the XRD results. Generally, small grain size is favorable for photocatalytic activation.[51]

In the TIOAg nanostructures, along with spatial charge separation and transfer from TiO_2 to Ag, the localized surface plasmon resonance (LSPR) is accountable for an enhanced photocatalytic activity. However, there are several possible mechanisms previously observed for the improved photocatalytic reactivity of metal-TiO_2 composite systems compared to pure TiO_2, including (i) enhancing the light absorption in the semiconductor via the radiative pathway, such as scattering[52] and (ii) direct transfer of plasmon-induced energy from the metal to the semiconductor to induce efficient charge separation in the semiconductor by non-radiative transfer mechanisms such as hot electron transfer (HET)[53] and plasmon-induced resonant energy transfer (PIRET).[54] Based on our results and previously reported literature, we propose PIRET as the main mechanism for the improved photocatalytic activity on the TIOAg samples as shown in Figure 8. Christopher et al.[55] thoroughly investigated and ruled out the direct injection of electrons from similar size AgNPs to the conduction band (CB) of TiO_2 in a Ag-TiO_2 system. Furthermore, the work-function position or Fermi level in Ag is similar in energy to the TiO_2 CB edge. In such case, any transfer of an electron from Ag to TiO_2 leads to electron-deficient AgNPs that are weak oxidizers and cannot accept electrons from water or C_2H_2.[56] According to the PIRET mechanism,[55] a strong plasmonic field would accumulate at the interface of TIOAg that can facilitate electronic excitation from the valence band (VB) of TiO_2 to Ti^{3+} defect states, which can then be further transferred to the CB of TiO_2 and eventually to Ag via spatial charge separation suppressing carrier recombination (Figure 8).[57,58] Typically, PIRET can usually be observed in larger plasmonic nanostructures (diameter > 50 nm)[59] and when the absorption edge tail of TiO_2 and the

plasmonic band of AgNPs overlap.[57] In the present work, the size of AgNPs was found to be more than 50 nm (TIOAg20x and 30x, Figure S2) and overlap of the absorption of TiO_2 and AgNPs occurred (Figure S5). Therefore, the PIRET pathway, which is given in equations 3-4:

$$TiO_2 + h\nu \rightarrow TiO_2\ (e^- + h^+) \quad (3)$$

$$AgNPs + TiO_2\ (e^- + h^+) \rightarrow AgNPs^-\ (e^-) + TiO_2\ (h^+) \quad (4)$$

PIRET

PIRET is proposed to be responsible for the photocatalytic degradation of C_2H_2 to CO_2 and H_2O (Fig. 8). The photoinduced electrons can be transferred to the abundant molecular oxygen via spatial charge separation from the TiO_2 to the Ag NPs, to form superoxide anion radicals ($O_2-\bullet$) as previously confirmed by electron spin resonance (ESR) spectroscopy,[60] whereas further protonation results in ($HO_2\bullet$) radicals. H_2O_2 is produced by the mixing of $HO_2\bullet$ radicals with the proton and electron.[55] On the other hand, holes in the VB of TiO_2 can react with water to produce •OH. These active species will induce oxidative degradation and mineralization of C_2H_2.[19,31] The generation of such reactive oxygen species (ROS) in TiO_2 with AgNPs has been extensively studied in the literature.[61,62]

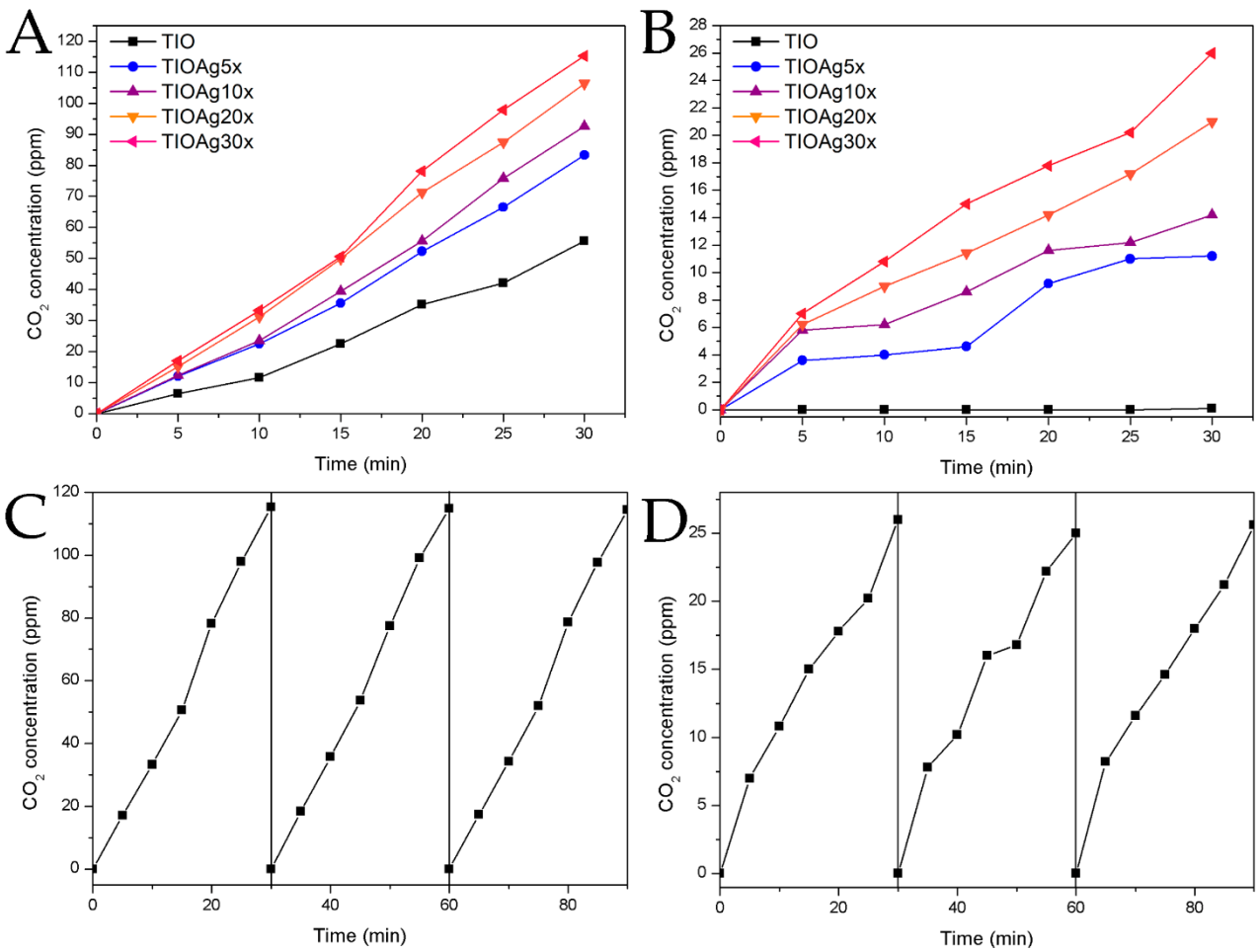

Figure 7. Photocatalytic activity results under (A, C) unfiltered, i.e. UV+Vis light, and (B, D) <390 nm filtered Xe lamp irradiation, i.e. mainly Vis light. (C) and (D) present reusability photocatalytic results for TIOAg30x.

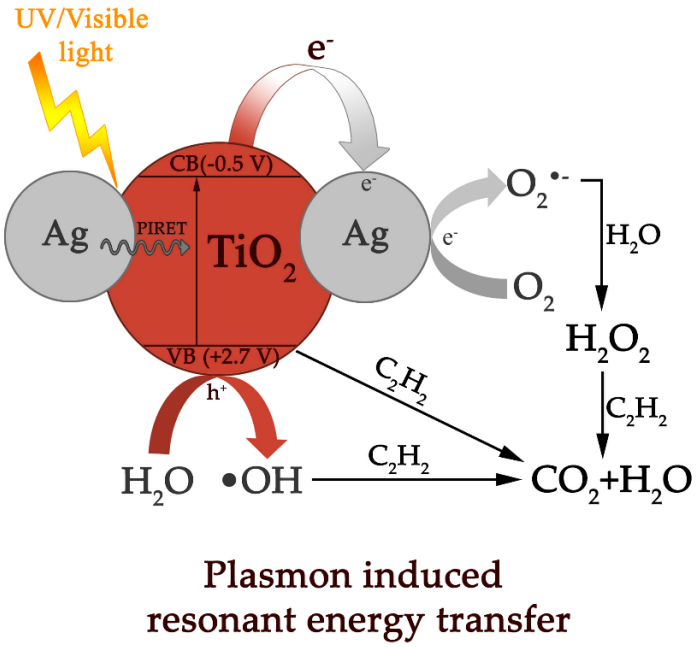

Figure 8. Schematic diagram of plasmon-induced resonant energy transfer process (PIRET) in TIOAg photocatalytic systems.

The photocatalytic activity was further evaluated for the hydrogen evolution from water vapor splitting under simulated sunlight (Figure 9A). Examination of TIO without nanoparticles revealed no hydrogen production due to its large band gap, low electron-hole pair separation and high recombination rate in the absences of electron acceptor/donor scavengers.[56] All samples which were decorated with AgNPs by LFS, however, demonstrated rather high hydrogen evolution yields, without use of a hole scavenger,[63] namely: TIOAg5x (14.9 µmol cm^{-2} h^{-1}), TIOAg10x (20 µmol cm^{-2} h^{-1}), TIOAg20x (24.6 µmol cm^{-2} h^{-1}) and TIOAg30x (32.9 µmol cm^{-2} h^{-1}). The enhanced hydrogen evolution is attributed to the deposition of AgNPs, as this increases with the amount of AgNPs.

We propose the H_2 evolution mechanism also follows the PIRET pathway because electron-deficient AgNPs may be too weak to oxidize water to O_2 as previously discussed.[56,64] Therefore, we propose the solar evolution of H_2 follows the scheme in Figure 9B. Upon light irradiation, TiO_2 IO generates electron-hole pairs via both direct and non-radiative excitation under UV light and PIRET excitation under visible light (both UV and Vis light are present in the simulated sunlight). The photoexcited electrons can be trapped by AgNPs, facilitating efficient electron-hole pair separation reducing the recombination rate. The oxidation potential of the holes in TiO_2 (+2.7 V vs. the standard hydrogen

electrode (SHE), pH=7) is enough for a successful water splitting (+0.83 V vs. SHE). The trapped electrons on AgNPs can take part of H_2 formation from $2H^+$ as follows:

$$TiO_2\ (h^+) + H_2O \rightarrow ½\ O_2 + 2H^+ \quad (5)$$

$$AgNPs^-\ (e^-) + 2H^+ \rightarrow H_2 + AgNPs \quad (6)$$

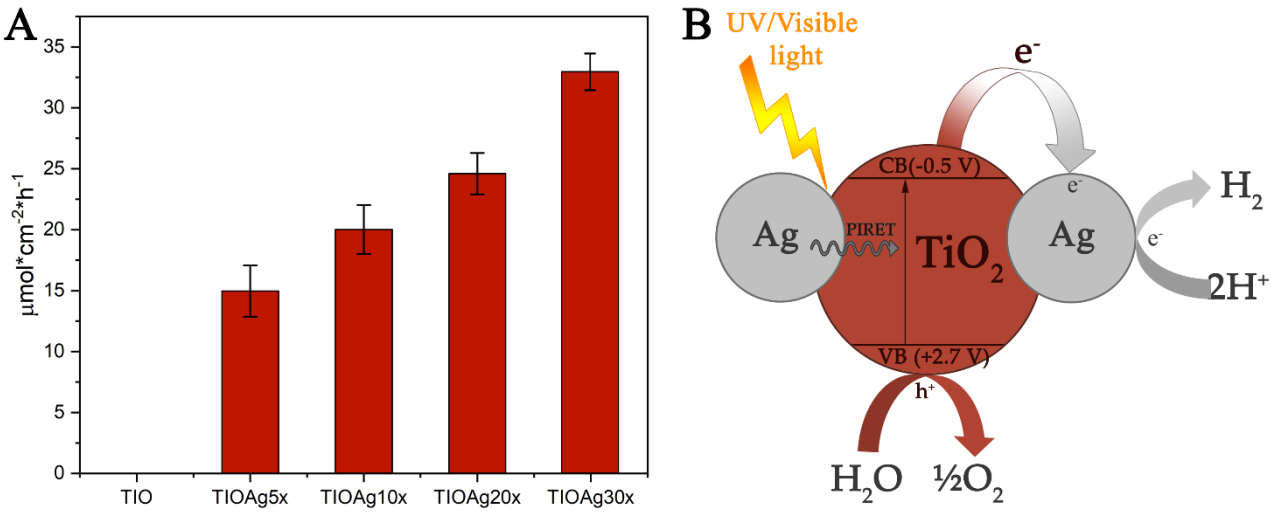

Figure 9. (A) H_2 evolution over the TIOAg with different AgNPs amounts under simulated sunlight and (B) a proposed mechanism for this solar H_2 evolution.

3 Conclusions

In conclusion, for the first time to our knowledge, we have demonstrated a facile deposition of Ag nanoparticles by a liquid flame spray (LFS) deposition process on TiO_2 inverse opal (TIO) structures. The deposition method allows efficient and rapid deposition with a high quality and uniform morphology of nanoparticles. Produced TIOAg photocatalysts were characterized by various analytical techniques such as XRD, EDS, Raman, UV and XPS spectroscopies, along with SEM, TEM and HRTEM microscopies. The photocatalytic activity was characterized by in-house built gas-phase reactors for the decomposition of C_2H_2 and for water splitting to produce H_2 gas. Functionalizing TIO with AgNPs significantly improves the gas phase photocatalytic degradation of C_2H_2 and the water splitting for hydrogen evolution, which can be attributed to energy transfer processes in metal/semiconductor junctions by plasmon-induced resonant energy transfer (PIRET). Our results show that a simple and cost-effective LFS deposition method is a suitable approach for producing silver-decorated TiO_2 inverse opal structures with enhanced gas phase photocatalytic

activity, even in the visible range. These results are expected to find applications in environmental and energy technologies.

4 Experimental section

4.1 Materials

Polystyrene (PS) spheres were prepared using distillated styrene (Acros Organics, 99%), ammonium persulfate (APS, Sigma-Aldrich, 98.0+%) and sodium dodecyl sulfate (SDS, Sigma-Aldrich, 98.5+%). Silver nitrate ($AgNO_3$, Sigma-Aldrich) and distilled water were used as a precursor for the preparation of AgNPs in the LFS deposition process. A titanium precursor solution was prepared by mixing titanium (IV) isopropoxide (TTIP, Sigma-Aldrich, ≥99%), hydrochloric acid (HCl, Merck, 37%), and ethanol (Altia, 99.5%). Microscopic glass slides (Thermo Scientific) were cleaned with piranha solution, washed with water and ethanol and dried before PS deposition.

4.2 Preparation of PS spheres

The preparation of polystyrene spheres (PS) was carried out according to Erola's procedure[65] with minor changes. Preparation of PS with an average diameter of 350 nm was performed in two steps: first PS seeds with average diameter 200 nm were prepared and subsequently they were grown to 350 nm. All chemicals were degassed before mixed in the reaction mixture. Firstly, 200 mg of sodium dodecyl sulfate (SDS) as a capping agent was poured into 160 mL of deionized water in a reaction vessel. This was stirred at 500 rpm using an anchor-like mixer and simultaneously heated up to 70°C. Then, styrene (20 g) was added. The reaction mixture was kept under stirring for 30 min at 70°C. Afterwards, 200 mg of ammonium persulfate (APS) dissolved in 20 ml of deionized water was quickly added into the reaction mixture as an initiator. The chemical reaction was kept for 20 h under nitrogen atmosphere, producing 200 nm PS seeds.

Secondly, distilled water (150 mL) and 30 mL of the colloidal PS seeds solution were loaded in a three-neck flask under nitrogen. Then, SDS (25 mg) was added to the mixture and the temperature increased up to 70°C. As soon as the temperature reached 70°C, APS (28 g) dissolved in 20 mL of deionized water was added to the reaction mixture. Finally, styrene (21.6 g) was added dropwise to the reaction mixture using a plastic syringe. The polymerization reaction was allowed to proceed at 70°C under nitrogen atmosphere for 20 h.

4.3 Preparation of TIO films

A three-step strategy was applied to prepare TIO films involving first the self-assembly of PS spheres, second the infiltration of TiO_2 precursor and finally the calcination (Figure 10). The microscopic glass slides were used as substrates for a PS film self-assembled deposition using a vertical deposition. Briefly, a PS suspension (1 ml) was diluted in 20 ml of distilled water in a 25 ml beaker. Two clamps were attached to the microscope glass slides and then carefully immersed vertically in such a way that they do not touch the beaker. The evaporation of the solution and its slow deposition on the glass surface was taking place in a laboratory oven for 2 days in the temperature range of 60–65°C.

Next, using a colloidal templated infiltration method TIO films were prepared. First, by mixing TTIP (1 ml), ethanol (1 ml) and 0.1M HCl (3 ml), a TiO_2 sol precursor was prepared. Then, this precursor solution was diluted 2 times with ethanol and stirred for 1 h before use. The microscopic glass slides with deposited PS films were immersed in TiO_2 precursor solution for 5 min and then dried in a fume hood for 24 h (room temperature) to complete hydrolyzation of the sol and formation of solid TiO_2. The resulting composites were calcined (high temperature treatment), when the drying process was finished, applying further protocol: heating from room temperature to 500°C in 9.5 h and holding for 4 h at 500°C to remove PS spheres and to convert TiO_2 into anatase crystalline phase. Finally, samples were cooled down naturally to room temperature. The observed active surface area with high quality TIO was 600 ± 25 mm^2 on the microscopic glass slide.

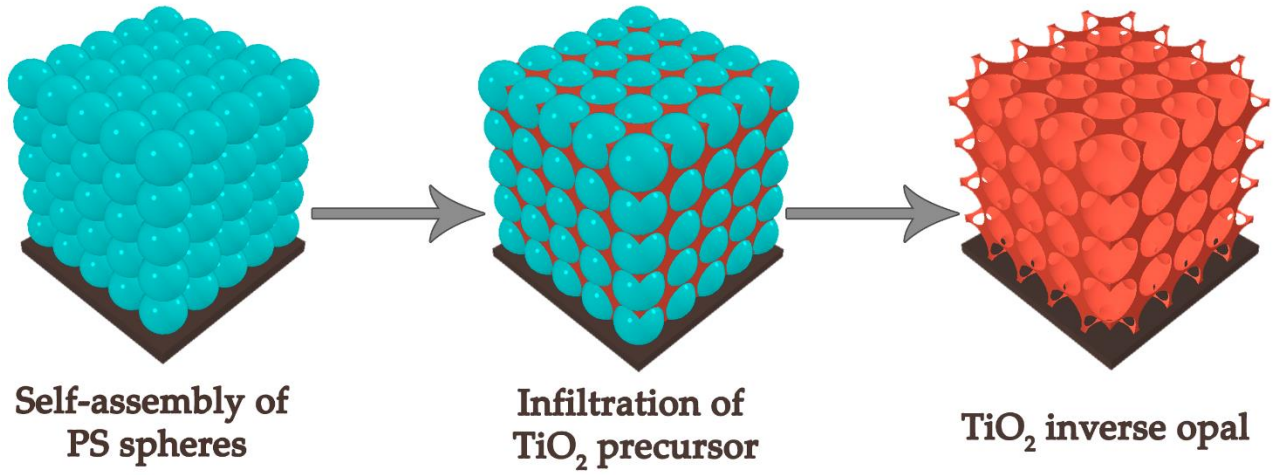

Figure 10. A schematic representation of the TIO preparation.

4.4 Liquid flame spray (LFS) deposition of silver nanoparticles

AgNPs were deposited using an LFS technique that allows a cost-efficient deposition of various metal and metal oxide nanoparticles in atmospheric conditions on large areas.[66,67] LFS contains a high temperature flame in which an organometallic precursor evaporates, nucleates, and forms solid nanoparticles of the final material (Figure 11). AgNPs nanoparticles were deposited on TIO structures using a rotating carousel and their amount was simply controlled by the number of times the TIO goes through the flame. The high temperature of the flame does not affect crystalline properties of used material since the exposure time is rather short; however, it does affect properties of already deposited nanoparticles. It has even been used to deposit particles on cellulose paper.[33] The LFS nozzle was placed 20 cm away from the sample surface. Hydrogen and oxygen were used for the combustion gases with gas flow rates of 20 L min^{-1} and 10 L min^{-1}, respectively. An additional nitrogen flow of 5 L min^{-1} was used as an inert sheath gas to modify the flame (burner design "KP").[68] The precursor, $AgNO_3$ dissolved in water (250 mg ml^{-1} of pure silver), was injected with a feed rate of 2 ml min^{-1} into the flame. The TIO structures were exposed to the depositing flame for 5, 10, 20, and 30 times (5x – 30x). The yield of the process, i.e., the relative number of deposited nanoparticles, is typically in the range of 10% to 50% depending on the substrate and the process parameters.[69]

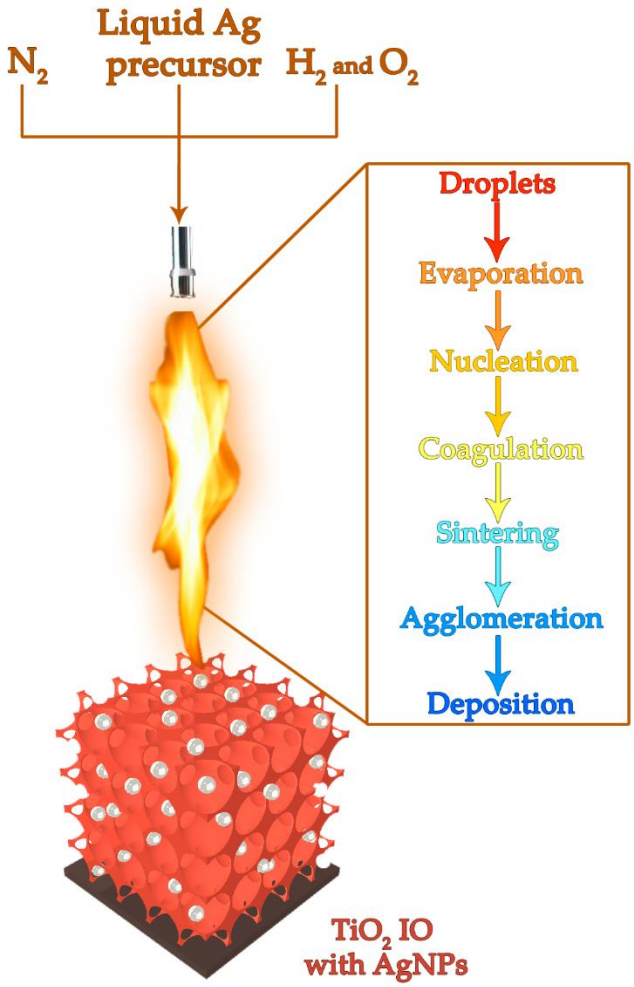

Figure 11. A schematic representation of the LFS deposition of AgNPs on TIO.

4.5 Characterization methods

The morphology and structure of the TIOAg samples were characterized using a Hitachi S-4800 FE-SEM (field emission scanning electron microscope). Transmission electron microscope (JEM-2100F, Jeol, Japan) micrographs of the TIO were acquired after drying a significantly diluted sample on a copper grid coated with lacey carbon film. The elemental identification of the TIOAg were obtained by energy dispersive X-ray spectroscopy (EDS) using the Noran system Six (NSS) software. The PerkinElmer Lambda 900 UV/Vis/NIR spectrometer fitted with a 150 mm integrating sphere was used to measure the diffuse absorbance spectra of the structures. Renishaw invia Raman microscope programmed with WireTM 3.4 software was used to confirm the preparation of TiO_2. The spectrum was measured using a 785 nm excitation laser with 1 mW power, an integration time of 10 s with measurement range of 100-800 cm^{-1}. The crystalline properties of the TiO_2 material were characterized with a Bruker-AXD D8 Advance device using CuKα as radiation source. The

diffraction patterns were measured between 12° and 90° at 2θ scale with a step size of 0.3° min^{-1} before and after the LFS deposition process. X-ray photoelectron spectroscopy (XPS) was used to determine the oxidation states of individual elements in the structures using a Thermo Scientific ESCALAB 250Xi system with an AlKα X-ray source**.**

4.6 Photocatalytic C_2H_2 degradation

An in-house built gas-phase photoreactor was employed for photocatalytic activity characterization on the degradation of C_2H_2 gas (Figure S7). Microscopic glass substrates with TIOAg were introduced in the photoreactor equipped with a UVA-transparent quartz window. A 450 W xenon lamp (OSRAM) was used for the irradiation (Figure S10). A filter composed of PMMA glass was used to block the < 390 nm light and produce mainly visible light (Figure S11). The xenon lamp was fixed at 20 cm above the reactor chamber so the intensity of the light at 300–800 nm was adjusted to 120 mW cm^{-2}, measured by a spectroradiometer (Gigahertz-Optik BTS256-LED). The excited photocatalytic material in the presence of UV-vis light decomposed C_2H_2 to CO_2. The concentration of CO_2 was directly detected by an optical detector (Vaisala GMP343 diffusion mode) inside the photoreactor.

4.7 Photocatalytic hydrogen evolution

Tests of photocatalytic hydrogen evolution from water vapor splitting were performed in a gas-tight system by using a glass sealed reactor (125 mL) with a quartz window.[70] A 300 W Xe arc lamp (including an AM 1.5 G filter) at a distance adjusted to obtain 1 sun (100 mW cm^{-2}) on the photocatalyst surface served as the light source to initiate the reaction. In a typical procedure, 10 ml of deionized water was poured on the bottom of reactor and microscopic glass slides with TIOAg were placed on top of a sample holder inside the reactor. The reactor was purged for 2 h with high purity He gas (10 ml min^{-1}) in order to remove air from reactor system. During the irradiation, water vapor serves as proton source for H_2 evolution (no hole scavengers were used). Periodically 500 µl of gas mixture from the reactor were withdrawn for quantitative analysis of products by a Shimadzu GCMS-2030 gas chromatograph fitted with Barrier Ionization Detector and He as a carrier gas. The products were calibrated with a standard gas mixture and determined by the retention time.

Supporting information

Supporting information contains SEM side-view images of the used PS template, the size distribution of AgNPs, SEM images of the large area of TiO_2 IO, EDS spectrum, XPS survey scan spectra of TIOAg5x, TIOAg10x and TIOAg20x, the schematic illustration of the gas-phase method, a plot of comparison of photocatalytic activities of TIO and TiO_2 NPs, HRTEM micrograph of TiO_2, the absorption spectrum of TiO_2 and AgNPs, the emission spectrum of the lamp, transmittance spectrum of PMMA filter and table for comparison of photocatalytic activities of TiO_2 IO structures.

Conflict of Interest

The authors declare no conflict of interest.

Acknowledgments

FT wishes to thank the Finnish Cultural Foundation for a research grant, Jari Leskinen from SIB lab, University of Eastern Finland for acquiring HRTEM micrographs, Centre for Physical Methods of Surface Investigation, Research Park of St. Petersburg State University, for help with conducting XPS measurements and Anitta Etula special grant from Saastamoinen Foundation for a travel grant. JJS acknowledges the Faculty of Science and Forestry at the University of Eastern Finland for the financial support (grant no. 579/2017) and the Academy of Finland Flagship for Photonics Research and Innovation (PREIN, decision no. 320166). SK and SE thank the EPSRC grants EP/S030727/1, EP/R035407/1 and EP/R035407/2 for financial support.

References

(1) United Nations Enviromnment Programme. Understanding the IPCC Special Report on 1.5°C. **2018**, 12.

(2) Wurfel, P. *Physics of Solar Cells: From Basic Principles to Advanced Concepts*, 2nd Editio.; WILEY-VCH, 2009.

(3) National Renewable Laboratory, “Best research cell efficiencies". National Renewable Laboratory, “Best Research Cell Efficiencies". *Metab. Eng.* 2018.

(4) Wang, S.; Xu, M.; Peng, T.; Zhang, C.; Li, T.; Hussain, I.; Wang, J.; Tan, B. Porous Hypercrosslinked Polymer-TiO2-Graphene Composite Photocatalysts for Visible-Light-Driven CO_2 Conversion. *Nat. Commun.* **2019**, *10*, 676.

(5) Fujishima, A.; N. Rao, T.; Tryk, D. Titanium Dioxide Photocatalysis. *J. Photochem. Photobiol. C Photochem. Rev.* **2000**, *1*, 1–21.

(6) Nakata, K.; Fujishima, A. TiO_2 Photocatalysis: Design and Applications. *J. Photochem. Photobiol. C Photochem. Rev.* **2012**, *13* (3), 169–189.

(7) Leytner, S.; Hupp, J. T. Evaluation of the Energetics of Electron Trap States at the Nanocrystalline Titanium Dioxide/Aqueous Solution Interface via Time-Resolved Photoacoustic Spectroscopy. *Chem. Phys. Lett.* **2000**, *330* (3–4), 231–236.

(8) Yue, X.; Pu, Y.; Zhang, W.; Zhang, T.; Gao, W. Ultrafine Pt Nanoparticles Supported on Double-Shelled C/TiO_2 Hollow Spheres Material as Highly Efficient Methanol Oxidation Catalysts. *J. Energy Chem.* **2020**, *49*, 275–282.

(9) Zhang, J.; Liu, Q.; He, H.; Shi, F.; Huang, G.; Xing, B.; Jia, J.; Zhang, C. Coal Tar Pitch as Natural Carbon Quantum Dots Decorated on TiO_2 for Visible Light Photodegradation of Rhodamine B. *Carbon N. Y.* **2019**, *152*, 284–294.

(10) Chen, Y.; Feng, L. Silver Nanoparticles Doped TiO_2 Catalyzed Suzuki-Coupling of Bromoaryl with Phenylboronic Acid under Visible Light. *J. Photochem. Photobiol. B Biol.* **2020**, *205* (November 2019), 111807–111817.

(11) Li, P.; Cao, Q.; Zheng, D.; Alshehri, A. A.; Alghamidi, Y. G.; Alzahrani, K. A.; Kim, M.; Hou, J.; Lai, L.; Yamauchi, Y.; Ide, Y.; Bando, Y.; Kim, J.; Malgras, V.; Lin, J. Synthesis of Mesoporous TiO_2-B Nanobelts with Highly Crystalized Walls toward Efficient H_2 Evolution. *Nanomaterials* **2019**, *9* (7), 919–928.

(12) Zheng, P.; Zhou, W.; Wang, Y.; Ren, D.; Zhao, J.; Guo, S. N-Doped Graphene-Wrapped TiO_2 Nanotubes with Stable Surface Ti_3^+ for Visible-Light Photocatalysis. *Appl. Surf. Sci.* **2019**, *512* (October 2019), 144549–1445551.

(13) Alfaro Cruz, M. R.; Sanchez-Martinez, D.; Torres-Martínez, L. M. TiO_2 Nanorods Grown by Hydrothermal Method and Their Photocatalytic Activity for Hydrogen Production. *Mater. Lett.* **2019**, *237*, 310–313.

(14) Liu, Y.; Zhou, M.; Zhang, W.; Chen, K.; Mei, A.; Zhang, Y.; Chen, W. Enhanced Photocatalytic Properties of TiO_2 Nanosheets@2D Layered Black Phosphorus Composite with High Stability under Hydro-Oxygen Environment. *Nanoscale* **2019**, *11* (12), 5674–5683.

(15) Poli, I.; Hintermair, U.; Regue, M.; Kumar, S.; Sackville, E. V.; Baker, J.; Watson, T. M.; Eslava, S.; Cameron, P. J. Graphite-Protected $CsPbBr_3$ Perovskite Photoanodes Functionalised with Water Oxidation Catalyst for Oxygen Evolution in Water. *Nat. Commun.* **2019**, *10* (1), 1–10.

(16) Sordello, F.; Duca, C.; Maurino, V.; Minero, C. Photocatalytic Metamaterials: TiO_2 Inverse Opals. *Chem. Commun.* **2011**, *47* (21), 6147–6149.

(17) Li, Y.; Piret, F.; Léonard, T.; Su, B. L. Rutile TiO_2 Inverse Opal with Photonic Bandgap in the UV-Visible Range. *J. Colloid Interface Sci.* **2010**, *348* (1), 280–288.

(18) Qi, D.; Lu, L.; Xi, Z.; Wang, L.; Zhang, J. Enhanced Photocatalytic Performance of TiO_2 Based on Synergistic Effect of Ti_3^+ Self-Doping and Slow Light Effect. *Appl. Catal. B Environ.* **2014**, *160–161* (1), 621–628.

(19) Temerov, F.; Ankudze, B.; Saarinen, J. J. TiO_2 Inverse Opal Structures with Facile Decoration of Precious Metal Nanoparticles for Enhanced Photocatalytic Activity. *Mater. Chem. Phys.* **2020**, *242* (February 2020), 122471–122477.

(20) Do, T.; Nguyen, D.; Nguyen, K.; Le, P. TiO2 and Au-TiO_2 Nanomaterials for Rapid Photocatalytic Degradation of Antibiotic Residues in Aquaculture Wastewater. *Materials (Basel).* **2019**, *2* (2434), 1–12.

(21) Barakat, M. A.; Al-Hutailah, R. I.; Qayyum, E.; Rashid, J.; Kuhn, J. N. Pt Nanoparticles/TiO_2 for Photocatalytic Degradation of Phenols in Wastewater. *Environ. Technol. (United Kingdom)* **2014**, *35* (2), 137–144.

(22) Boppella, R.; Kochuveedu, S. T.; Kim, H.; Jeong, M. J.; Mota, F. M.; Park, J. H.; Kim, D. H. Plasmon-Sensitized Graphene/TiO_2 Inverse Opal Nanostructures with Enhanced Charge Collection Efficiency for Water Splitting. *ACS Appl. Mater. Interfaces* **2017**, *9*, 7075–7083.

(23) Yu, J.; Lei, J.; Wang, L.; Zhang, J.; Liu, Y. TiO_2 Inverse Opal Photonic Crystals : Synthesis , Modification , and Applications - A Review. *J. Alloys Compd.* **2018**, *769*, 740–757.

(24) Qi, D.; Lu, L.; Wang, L.; Zhang, J. Improved SERS Sensitivity on Plasmon-Free TiO_2 Photonic Microarray by Enhancing Light-Matter Coupling. *J. Am. Chem. Soc.* **2014**, *136* (28), 9886–9889.

(25) Eftekhari, E.; Broisson, P.; Aravindakshan, N.; Wu, Z.; Cole, I. S.; Li, X.; Zhao, D.; Li, Q. Sandwich-Structured TiO_2 Inverse Opal Circulates Slow Photons for Tremendous Improvement in Solar Energy Conversion Efficiency. *J. Mater. Chem. A* **2017**, *5* (25), 12803–12810.

(26) Zhang, X. F.; Liu, Z. G.; Shen, W.; Gurunathan, S. Silver Nanoparticles: Synthesis, Characterization, Properties, Applications, and Therapeutic Approaches. *Int. J. Mol. Sci.* **2016**, *17* (9), 1–34.

(27) Wahyuni, E. T.; Roto, R. Silver Nanoparticle Incorporated Titanium Oxide for Bacterial Inactivation and Dye Degradation. In *Titanium Dioxide - Material for a Sustainable*

Environment; 2018; pp 1–18. DOI: 10.5772/intechopen.75918.

(28) Sirivallop, A.; Areerob, T.; Chiarakorn, S. Enhanced Visible Light Photocatalytic Activity of N and Ag Doped and Co-Doped TiO_2 Synthesized by Using an In-Situ Solvothermal Method for Gas Phase Ammonia Removal. *Catalysis* **2020**, *10* (2), 1–18.

(29) Assaud, L.; Brazeau, N.; Barr, M. K. S.; Hanbücken, M.; Ntais, S.; Baranova, E. A.; Santinacci, L. Atomic Layer Deposition of Pd Nanoparticles on TiO_2 Nanotubes for Ethanol Electrooxidation: Synthesis and Electrochemical Properties. *ACS Appl. Mater. Interfaces* **2015**, *7* (44), 24533–24542.

(30) Hamdi, S. S. Synthesis of Ag –TiO_2 Thin Films by Spin Coating Process. *Eng. &Tech.Journal* **2016**, *34-A* (13), 2443–2449.

(31) Chen, Z.; Fang, L.; Dong, W.; Zheng, F.; Shen, M.; Wang, J. Inverse Opal Structured Ag/TiO_2 Plasmonic Photocatalyst Prepared by Pulsed Current Deposition and Its Enhanced Visible Light Photocatalytic Activity. *J. Mater. Chem. A* **2014**, *2* (3), 824–832.

(32) Ejenstam, L.; Tuominen, M.; Haapanen, J.; Mäkelä, J. M.; Pan, J.; Swerin, A.; Claesson, P. M. Long-Term Corrosion Protection by a Thin Nano-Composite Coating. *Appl. Surf. Sci.* **2015**, *357*, 2333–2342.

(33) Tuominen, M.; Teisala, H.; Aromaa, M.; Stepien, M.; Mäkelä, J. M.; Saarinen, J. J.; Toivakka, M.; Kuusipalo, J. Creation of Superhydrophilic Surfaces of Paper and Board. *J. Adhes. Sci. Technol.* **2014**, *28* (8–9), 864–879.

(34) Mäkelä, J. M.; Keskinen, H.; Forsblom, T.; Keskinen, J. Generation of Metal and Metal Oxide Nanoparticles by Liquid Flame Spray Process. *J. Mater. Sci.* **2004**, *39* (8), 2783–2788.

(35) Sorvali, M.; Vuori, L.; Pudas, M.; Haapanen, J.; Mahlberg, R.; Ronkainen, H.; Honkanen, M.; Valden, M.; Makela, J. M. Fabrication of Ultrathin Multilayered Superomniphobic

Nanocoatings by Liquid Flame Spray, Atomic Layer Deposition, and Silanization. *Nanotechnology* **2018**, *29* (18), 185708.

(36) Temerov, F.; Ammosova, L. Protective Stainless Steel Micropillars for Enhanced Photocatalytic Activity of TiO_2 Nanoparticles during Wear. *Surf. Coat. Technol.* **2020**, *381* (15), 125201–125208.

(37) Mohapatra, P.; Shaw, S.; Mendivelso-Perez, D.; Bobbitt, J. M.; Silva, T. F.; Naab, F.; Yuan, B.; Tian, X.; Smith, E. A.; Cademartiri, L. Calcination Does Not Remove All Carbon from Colloidal Nanocrystal Assemblies. *Nat. Commun.* **2017**, *8* (1), 1–7.

(38) Barman, B.; Dhasmana, H.; Verma, A.; Kumar, A.; Chaudhary, S. P.; Jain, V. K. Formation of Plasmonic Silver Nanoparticles Using Rapid Thermal Annealing at Low Temperature and Study in Reflectance Reduction of Si Surface. *Adv. Nat. Sci. Nanosci. Nanotechnol.* **2017**, *8* (3), 1–8.

(39) Liu, J.; Li, M.; Zhou, J.; Ye, C.; Wang, J.; Jiang, L.; Song, Y.; Liu, J.; Li, M.; Zhou, J.; Ye, C.; Wang, J.; Jiang, L. Reversibly Phototunable TiO_2 Photonic Crystal Modulated by Ag Nanoparticles ' Oxidation / Reduction. *Appl. Phys. Lett.* **2014**, *98*, 023110–023113.

(40) Huo, J.; Yuan, C.; Wang, Y. Nanocomposites of Three-Dimensionally Ordered Porous TiO_2 Decorated with Pt and Reduced Graphene Oxide for the Visible-Light Photocatalytic Degradation of Waterborne Pollutants. *ACS Appl. Nano Mater.* **2019**, *2* (5), 2713–2724.

(41) Grouchko, M.; Kamyshny, A.; Mihailescu, C. F.; Anghel, D. F.; Magdassi, S. Conductive Inks with a "Built-in" Mechanism That Enables Sintering at Room Temperature. *ACS Nano* **2011**, *5* (4), 3354–3359.

(42) Leong, K. H.; Gan, B. L.; Ibrahim, S.; Saravanan, P. Synthesis of Surface Plasmon Resonance (SPR) Triggered Ag/TiO_2 Photocatalyst for Degradation of Endocrine Disturbing Compounds.

Appl. Surf. Sci. **2014**, *319* (1), 128–135.

(43) Zhang, Z.; Zhang, L.; Hedhili, M. N.; Zhang, H.; Wang, P. Plasmonic Gold Nanocrystals Coupled with Photonic Crystal Seamlessly on TiO_2 Nanotube Photoelectrodes for Efficient Visible Light Photoelectrochemical Water Splitting. *Nano Lett.* **2013**, No. 13, 14–20.

(44) Wang, T.; Yan, X.; Zhao, S.; Lin, B.; Xue, C.; Yang, G.; Ding, S.; Yang, B.; Ma, C.; Yang, G.; Yang, G. A Facile One-Step Synthesis of Three-Dimensionally Ordered Macroporous N-Doped TiO_2 with Ethanediamine as the Nitrogen Source. *J. Mater. Chem. A* **2014**, *2* (37), 15611–15619.

(45) Chen, D.; Chen, Q.; Ge, L.; Yin, L.; Fan, B.; Wang, H.; Lu, H.; Xu, H.; Zhang, R.; Shao, G. Synthesis and Ag-Loading-Density-Dependent Photocatalytic Activity of Ag@TiO_2 Hybrid Nanocrystals. *Appl. Surf. Sci.* **2013**, *284*, 921–929.

(46) Yan, X.; Ohno, T.; Nishijima, K.; Abe, R.; Ohtani, B. Is Methylene Blue an Appropriate Substrate for a Photocatalytic Activity Test? A Study with Visible-Light Responsive Titania. *Chem. Phys. Lett.* **2006**, *429* (4–6), 606–610.

(47) Thevenet, F.; Guaitella, O.; Puzenat, E.; Herrmann, J. M.; Rousseau, A.; Guillard, C. Oxidation of Acetylene by Photocatalysis Coupled with Dielectric Barrier Discharge. *Catal. Today* **2007**, *122* (1–2), 186–194.

(48) Zulfiqar, A.; Temerov, F.; Saarinen, J. J. Multilayer TiO_2 Inverse Opal with Gold Nanoparticles for Enhanced Photocatalytic Activity. *ACS Omega* **2020**, *5* (20), 11595–11604.

(49) Chen, X.; Ye, J.; Ouyang, S.; Kako, T.; Li, Z.; Zou, Z. Enhanced Incident Photon-to-Electron Conversion Efficiency of Tungsten Trioxide Photoanodes Based on 3d-Photonic Crystal Design. *ACS Nano* **2011**, *5* (6), 4310–4318.

(50) Calza, P.; Minella, M.; Demarchis, L.; Sordello, F.; Minero, C. Photocatalytic Rate

Dependence on Light Absorption Properties of Different TiO_2 Specimens. *Catal. Today* **2020**, *340* (July 2020), 12–18.

(51) Wu, M.; Jin, J.; Liu, J.; Deng, Z.; Li, Y.; Deparis, O.; Su, B. L. High Photocatalytic Activity Enhancement of Titania Inverse Opal Films by Slow Photon Effect Induced Strong Light Absorption. *J. Mater. Chem. A* **2013**, *1* (48), 15491–15500.

(52) Islam, K.; Alnuaimi, A.; Battal, E.; Okyay, A. K.; Nayfeh, A. Effect of Gold Nanoparticles Size on Light Scattering for Thin Film Amorphous-Silicon Solar Cells. *Sol. Energy* **2014**, *103*, 263–268.

(53) Khan, M. R.; Chuan, T. W.; Yousuf, A.; Chowdhury, M. N. K.; Cheng, C. K. Schottky Barrier and Surface Plasmonic Resonance Phenomena towards the Photocatalytic Reaction: Study of Their Mechanisms to Enhance Photocatalytic Activity. *Catal. Sci. Technol.* **2015**, *5* (5), 2522–2531.

(54) Erwin R. William, Zarick F. Holly, T. M. E. and B. R. Light Trapping in Mesoporous Solar Cells with Plasmonic Nanostructures. *Energy Environ. Sci.* **2016**, No. 9, 1577–1601.

(55) Christopher, P.; Ingram, D. B.; Linic, S. Enhancing Photochemical Activity of Semiconductor Nanoparticles with Optically Active Ag Nanostructures: Photochemistry Mediated by Ag Surface Plasmons. *J. Phys. Chem. C* **2010**, *114* (19), 9173–9177.

(56) Varapragasam, S. J. P.; Mia, S.; Wieting, C.; Balasanthiran, C.; Hossan, M. Y.; Baride, A.; Rioux, R. M.; Hoefelmeyer, J. D. Ag-TiO_2 Hybrid Nanocrystal Photocatalyst: Hydrogen Evolution under UV Irradiation but Not under Visible-Light Irradiation. *ACS Appl. Energy Mater.* **2019**, *2* (11), 8274–8282.

(57) Cushing, S. K.; Li, J.; Bright, J.; Yost, B. T.; Zheng, P.; Bristow, A. D.; Wu, N. Controlling Plasmon-Induced Resonance Energy Transfer and Hot Electron Injection Processes in

Metal@TiO_2 Core-Shell Nanoparticles. *J. Phys. Chem. C* **2015**, *119* (28), 16239–16244.

(58) Li, J.; Cushing, S. K.; Meng, F.; Senty, T. R.; Bristow, A. D.; Wu, N. Plasmon-Induced Resonance Energy Transfer for Solar Energy Conversion. *Nat. Photonics* **2015**, *9* (9), 601–607.

(59) Burda, C.; Chen, X.; Narayanan, R.; El-sayed, M. A. Chemistry and Properties of Nanocrystals of Different Shapes. *Chem. Commun.* **2005**, *105* (4), 1025–1102.

(60) Hirakawa, T.; Kominami, H.; Ohtani, B.; Nosaka, Y. Mechanism of Photocatalytic Production of Active Oxygens on Highly Crystalline TiO_2 Particles by Means of Chemiluminescent Probing and ESR Spectroscopy. *J. Phys. Chem. B* **2001**, *105* (29), 6993–6999.

(61) Szabó-Bárdos, E.; Pétervári, E.; El-Zein, V.; Horváth, A. Photocatalytic Decomposition of Aspartic Acid over Bare and Silver Deposited TiO_2. *J. Photochem. Photobiol. A Chem.* **2006**, *184* (1–2), 221–227.

(62) Nosaka, Y.; Nosaka, A. Y. Generation and Detection of Reactive Oxygen Species in Photocatalysis. *Chem. Rev.* **2017**, *117* (17), 11302–11336.

(63) Jo, W. K.; Kumar, S.; Eslava, S.; Tonda, S. Construction of Bi_2WO_6/RGO/g-C_3N_4 2D/2D/2D Hybrid Z-Scheme Heterojunctions with Large Interfacial Contact Area for Efficient Charge Separation and High-Performance Photoreduction of CO_2 and H_2O into Solar Fuels. *Appl. Catal. B Environ.* **2018**, *239* (August), 586–598.

(64) Awazu, K.; Fujimaki, M.; Rockstuhl, C.; Tominaga, J.; Murakami, H.; Ohki, Y.; Yoshida, N.; Watanabe, T. A Plasmonic Photocatalyst Consisting of Silver Nanoparticles Embedded in Titanium Dioxide. *J. Am. Chem. Soc.* **2008**, *130* (5), 1676–1680.

(65) Erola, M. O. A.; Philip, A.; Ahmed, T.; Suvanto, S.; Pakkanen, T. T. Journal of Solid State Chemistry Fabrication of Au- and Ag – SiO_2 Inverse Opals Having Both Localized Surface

Plasmon Resonance and Bragg Diffraction. *J. Solid State Chem.* **2015**, *230*, 209–217.

(66) Stepien, M.; Saarinen, J. J.; Teisala, H.; Tuominen, M.; Aromaa, M.; Kuusipalo, J.; Mäkelä, J. M.; Toivakka, M. Surface Chemical Characterization of Nanoparticle Coated Paperboard. *Appl. Surf. Sci.* **2012**, *258* (7), 3119–3125.

(67) Brobbey, K. J.; Haapanen, J.; Gunell, M.; Mäkelä, J. M.; Eerola, E.; Toivakka, M.; Saarinen, J. J. One-Step Flame Synthesis of Silver Nanoparticles for Roll-to-Roll Production of Antibacterial Paper. *Appl. Surf. Sci.* **2017**, *420*, 558–565.

(68) Aromaa, M.; Keskinen, H.; Mäkelä, J. M. The Effect of Process Parameters on the Liquid Flame Spray Generated Titania Nanoparticles. *Biomol. Eng.* **2007**, *24* (5), 543–548.

(69) Haapanen, J.; Aromaa, M.; Teisala, H.; Tuominen, M.; Stepien, M.; Saarinen, J. J. Binary TiO_2/SiO_2 Nanoparticle Coating for Controlling the Wetting Properties of Paperboard. *Mater. Chem. Phys.* **2015**, *150*, 230–237.

(70) Kumar, S.; Regue, M.; Isaacs, M. A.; Freeman, E.; Eslava, S. All-Inorganic $CsPbBr_3$ Nanocrystals: Gram-Scale Mechanochemical Synthesis and Selective Photocatalytic CO_2 Reduction to Methane. *ACS Appl. Energy Mater.* **2020**, *3* (5), 4509–4522.

TOC

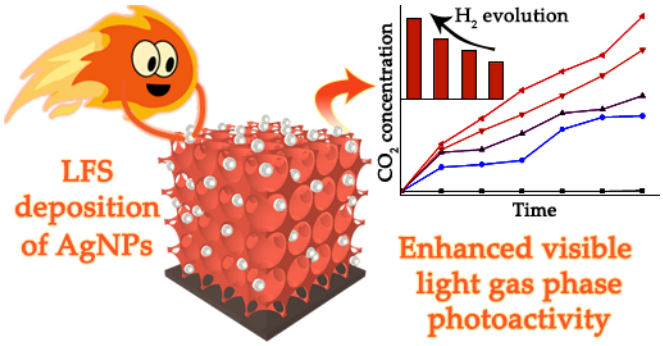
LFS
deposition
of AgNPs
H_2 evolution
CO_2 concentration
Time
Enhanced visible
light gas phase
photoactivity